

On the Location of Boron in SiO₂-Embedded Si Nanocrystals—An X-ray Absorption Spectroscopy and Density Functional Theory Study

Daniel Hiller,* Dirk König,* Peter Nagel, Michael Merz, Stefan Schuppler, and Sean C. Smith

Doping of silicon nanostructures is crucial to understand their properties and to enhance their potential in various fields of application. Herein, SiO₂-embedded Si nanocrystals (quantum dots) $\approx 3\text{--}6$ nm in diameter are used as a model system to study the incorporation of B dopants by X-ray absorption near-edge spectroscopy (XANES). Such samples represent a model system for ultimately scaled, 3D-confined Si nanovolumes. The analysis is complemented by real-space density functional theory to calculate the 1s (K shell) electron binding energies of B in 11 different, thermodynamically stable configurations of the Si/SiO_x/SiO₂ system. Although no indications for a substitutional B-acceptor configuration are found, the predominant O coordination of B indicates the preferred B incorporation into the SiO₂ matrix and near the Si-nanocrystal/SiO₂ interface, which is inherently incompatible with charge carrier generation by dopants. It is concluded that B doping of ultrasmall Si nanostructures fails due to a lack of B incorporation onto Si lattice sites that cannot be overcome by increasing the B concentration. The inability to efficiently insert B into Si nanovolumes appears to be a boron-specific fundamental obstacle for electronic doping (e.g., not observed for phosphorus) that adds to the established nanosize effects, namely, increased dopant activation and ionization energies.

1. Introduction

The incorporation of boron (B) impurities into ultrasmall silicon nanocrystals (Si NCs) and other Si nanovolumes is technically not trivial and its efficient feasibility is still a matter of debate. The first reports about B-doped Si NCs attributed photoluminescence (PL) quenching to nonradiative Auger recombination of excitons with doping-induced free carriers.^[1] Meanwhile, several reports support the concept that Si NCs ≤ 6 nm in diameter are not electronically p-type-doped (i.e., possess free carriers from B dopants) but that B in the NCs or the surrounding SiO₂ creates nonradiative defect states.^[2–5]

The situation is further complicated by the preferential incorporation of B on or near the surface of Si NCs as demonstrated in theoretical and experimental work.^[3,6–11] In such configurations, the substitutional incorporation of B on Si lattice sites with exclusive first next-neighbor (1nn) Si atoms as a mandatory requirement for electronic

doping are extremely unlikely. In contrast, significant free-carrier densities and plasmonic behavior were observed for excessive B

Dr. D. Hiller
Chair of Nanoelectronics
Institute of Semiconductors and Microsystems (IHM)
Technische Universität Dresden
01187 Dresden, Germany
E-mail: daniel.hiller@mailbox.tu-dresden.de

Dr. D. Hiller
Research School of Engineering
Australian National University (ANU)
Canberra, ACT 2601, Australia

 The ORCID identification number(s) for the author(s) of this article can be found under <https://doi.org/10.1002/pssb.202000623>.

© 2021 The Authors. Physica Status Solidi B published by Wiley-VCH GmbH. This is an open access article under the terms of the Creative Commons Attribution-NonCommercial License, which permits use, distribution and reproduction in any medium, provided the original work is properly cited and is not used for commercial purposes.

DOI: 10.1002/pssb.202000623

Dr. D. König, Prof. S. C. Smith
Integrated Materials Design Lab (IMDL)
Australian National University (ANU)
Canberra, ACT 2601, Australia
E-mail: solidstatedirk@gmail.com

Dr. D. König
Integrated Materials Design Centre (IMDC)
University of New South Wales (UNSW)
Sydney, NSW 2052, Australia

Dr. P. Nagel, Dr. M. Merz, Dr. S. Schuppler
Institute for Quantum Materials and Technologies (IQMT)
Karlsruhe Institute of Technology (KIT)
76021 Karlsruhe, Germany

Prof. S. C. Smith
Department of Applied Mathematics
Research School of Physics
Australian National University (ANU)
Canberra, ACT 2601, Australia

concentrations in Si NCs (hyperdoping).^[12–14] However, such B concentrations induce a phase transition from B-doped Si to Si borides.^[15]

In this work, we study in theory and experiment the chemical environment of B in the Si NC/SiO₂ system to investigate the local atomic surroundings of B atoms and the preferential sites for their incorporation. For this purpose, we combine X-ray absorption near-edge spectroscopy (XANES) at the B K-edge with density functional theory (DFT).

2. Results

Table 1 gives an overview on the configuration of all B-doped Si NC/SiO₂ samples investigated here as well as the B-doped SiO₂ and bulk-Si reference samples.

Figure 1 shows PL spectra of the Si NC samples. For the nominally 3 nm NC-size samples PL peaks at 765 nm are observed, irrespective of low (0.47 at%) or high (1.32 at%) B concentration. In contrast, the nominally 6 nm NC-size samples with low B concentration have a typical peak position at 905 nm, which shifts to 855 nm for high B concentration. We attribute this PL blueshift to a slightly lower excess-Si concentration in highly B-doped Si-rich oxide layers (cf., secondary ion mass spectrometry (SIMS) quantification data in Hiller et al.^[3]), which causes a slightly reduced average Si NC size. It was also shown that high B concentrations in SRO precursor layers hamper the NC formation during annealing, resulting in a reduced NC size.^[16] In addition, the preferential incorporation of near-interfacial B atoms into larger NCs (as recently reported by Demoulin et al.)^[11] could also contribute to the PL blueshift when the formation of B-induced luminescence quenching defects is considered.^[3] As expected, no PL signal is measured for the SiO₂:B reference samples that do not contain any Si NCs (black curves in Figure 1).

The PL intensities of both NC sizes (not shown) drop to $\approx 14\%$ when going from low to high B concentrations. As shown before, this PL loss is mainly attributed to B-induced defects and is not an indication of Auger quenching by B-induced free carriers.^[3,4]

For XANES measurements, we initially used a highly B-doped Si wafer reference sample (0.005–0.015 Ω cm, corresponding to a

Table 1. Overview of the samples used in this study. The suffixes -L and -H in the sample names denote low and high B concentrations, respectively. In the Si NC/SiO₂ bilayer samples initially only the Si-rich oxide (SRO) layers contained boron, which, however, diffused during the high-temperature annealing required to form the Si NCs (diffusion length ≈ 7 nm).^[9] For comparison with the samples with homogeneous B distribution, the last column shows the average B concentration in the XANES-probed sample volume.

Sample	Configuration	Avg. [B] [at%]
3 nm-L	50 × [(3 nm SiO ₂) + (3 nm SRO:B @ 0.47 at%)]	0.24
6 nm-L	50 × [(3 nm SiO ₂) + (6 nm SRO:B @ 0.47 at%)]	0.31
3 nm-H	50 × [(3 nm SiO ₂) + (3 nm SRO:B @ 1.32 at%)]	0.66
6 nm-H	50 × [(3 nm SiO ₂) + (6 nm SRO:B @ 1.32 at%)]	0.88
SiO ₂ :B-L	225 nm SiO ₂ :B @ 0.25 at%	0.25
SiO ₂ :B-H	225 nm SiO ₂ :B @ 0.8 at%	0.8
Si:B	B-implanted Si wafer (0.2 at% near surface; 19 Ω \square^{-1})	0.2

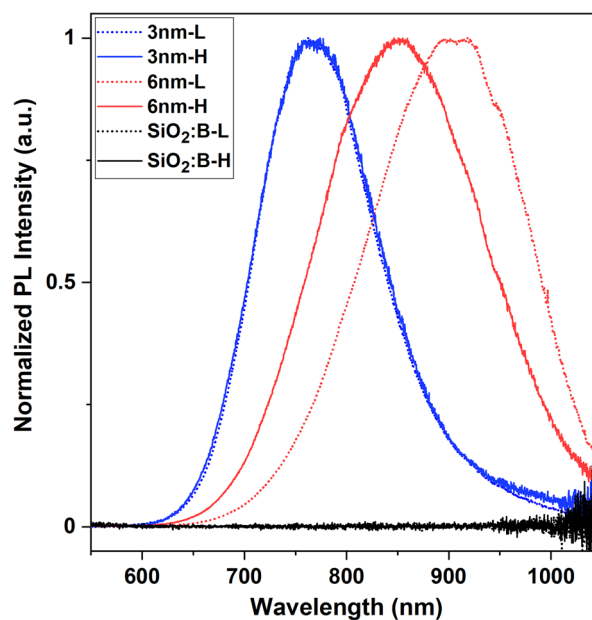


Figure 1. Normalized room-temperature PL spectra of B-incorporating Si NC/SiO₂ samples and SiO₂:B reference samples. The suffixes -L and -H denote the low (-L) and high (-H) B concentrations.

B concentration of 1.2×10^{19} – 3×10^{18} cm⁻³) but failed to reveal any significant X-ray absorption peaks. Therefore, a Si wafer was B implanted to obtain a higher B concentration. In **Figure 2** a depth profile of the active B concentration in sample Si:B is plotted, which shows an ≈ 200 nm deep plateau under the surface with $\approx 1 \times 10^{20}$ cm⁻³, before its slow decline. We identify this active B concentration with the total B concentration because the postimplantation anneal was conducted at 1000 °C for

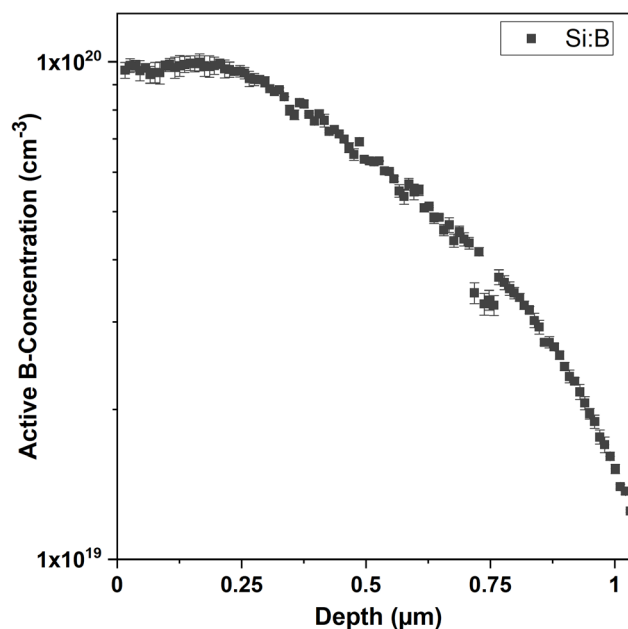


Figure 2. Electrochemical capacitance–voltage (ECV) depth profile of the active B concentration in the B-implanted Si-wafer reference sample (Si:B).

30 min, being sufficient to activate all B dopants in silicon.^[17] The absorption length of ≈ 200 eV X-rays (i.e., near the B K-edge) in Si (or SiO₂) is ≈ 100 nm. Therefore, $>95\%$ of the incident beam is absorbed in the highly B-doped plateau of the Si:B sample. A comparatively large amount of the incident beam is also absorbed in the active layers of the Si NC and SiO₂:B reference samples.

The XANES spectra near the B K-edge of all samples are shown in Figure 3a. One peak is observed at 192 eV and occurs very prominently for sample 6 nm-H but is also weakly visible for samples 3 nm-H. Reference sample Si:B exhibits this peak only very faintly. This peak has been attributed in the literature to B dimers and configurations involving B–B bonds and is known to occur only at high B concentrations.^[18–20] Therefore, this peak marks the onset of B clustering, which implicates that a significant fraction of boron is present in a configuration that is inherently incompatible with B doping. Concerning the peak intensities, an ≈ 10 times higher fluorescence yield is observed for samples 6 nm-H compared to 3 nm-H, although the B concentration in the initial SRO layers was identical. However, the number of Si atoms constituting the nominally 3 nm diameter Si NCs is just $1/8$ of the nominally 6 nm Si NCs. At a constant B concentration, there is therefore an eight times lower probability for B-dimer formation, which explains the peak intensity difference. Furthermore, cluster analysis of atom probe tomography data^[3] demonstrates that the number of B impurities in Si NCs scales with the NC size so that at least two B atoms in one NC (prerequisite for a dimer) are predominantly found in larger NCs.

As shown more clearly in Figure 3b, only the Si NC samples with high B concentration (6 nm-H, 3 nm-H to some degree) exhibit shoulders at 193.4 and 193.65 eV, which we attribute to B at the Si NC/SiO₂ interface or the Si-rich oxide transition shell around the Si NCs; see below for the assignment of XANES peaks to core level energies from DFT and associated discussion.

The most intense peak found in all samples is located at 194.25 eV. Even the sample set with low B concentration (3 nm-L, 6 nm-L, SiO₂:B-L) clearly shows this peak. However, in the Si:B reference sample that peak only reaches a fluorescence yield that is at least one order of magnitude lower than for the other samples, despite comparable B concentration (cf., Table 1). Also, that peak occurs for the SiO₂:B reference samples with comparable intensity as for the B-doped Si NC/SiO₂ samples, which strongly suggests that it corresponds to B in SiO₂. Thus, in the Si:B reference sample the peak originates from B atoms in the (typically ≈ 2 nm thick) native surface oxide, which explains its low intensity as compared to the >200 nm thick deposited layers. The attribution of the 194.25 eV peak to tetrahedral O-coordinated B atoms in SiO₂ is supported by X-ray absorption spectra of B₂O₃–SiO₂ glasses^[21] or B-zeolites B(OSi)₄ and B(OSi)₃.^[22]

All the deposited samples with high B concentration (3 nm-H, 6 nm-H, SiO₂:B-H) show two weak and broad features at 200 and 204 eV, which have been attributed to tetrahedral and trigonal B₂O₃ phases before.^[21,22] This observation is another indication for the segregation of boron into new phases in sample set “-H” with high B concentration, though its occurrence is scarce as compared to B incorporation into SiO₂.

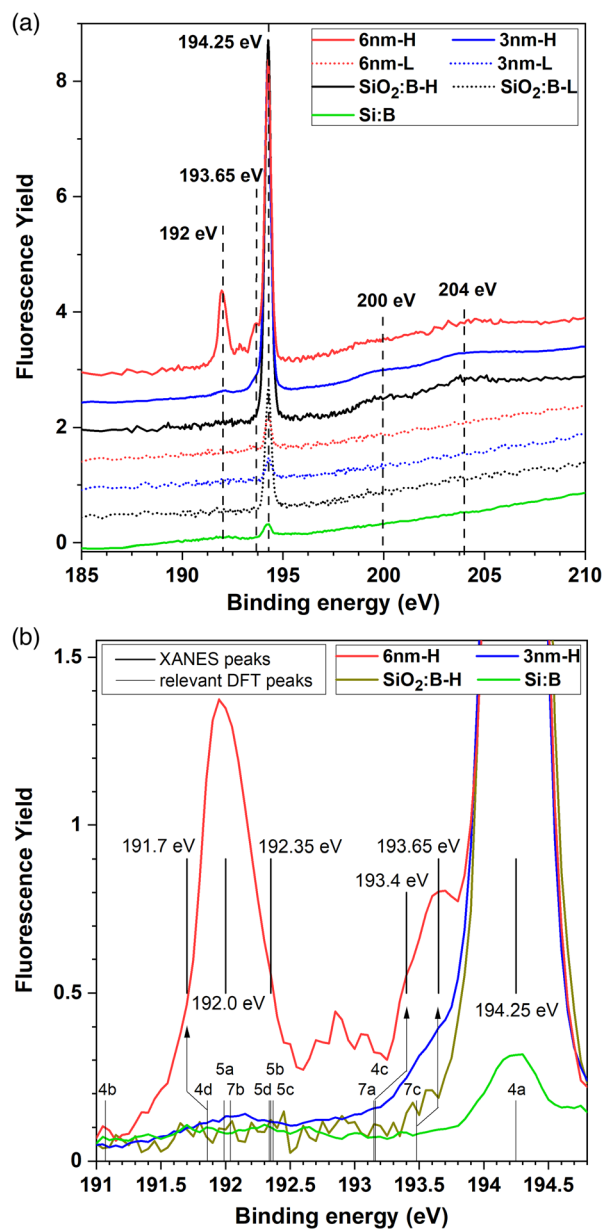


Figure 3. Boron K-edge X-ray absorption spectra (fluorescence yield). a) Spectra of all samples offset by 0.5 each for the sake of better visibility. The dashed lines indicate the peaks discussed in the text. b) Zoomed-in and unstacked region on the low-energy side of the most prominent 194.25 eV peak of all “-H” samples with high B concentration. Thick black lines show peaks and shoulders of XANES signals $E_K(B)$, thin black lines show $E_{1s\uparrow}(B)$ derived from DFT calculations and calibrated to experiment; see text for details. Combined number–letter labels refer to respective graphs in Figure 4, 5, and 7, and to respective rows in Table 2.

3. Discussion

DFT calculations with Gaussian-type all-electron molecular orbital basis sets (MO-BSs) present a vital theoretical method to interpret XANES spectra.^[23] Unlike in effective core-potential (ECP) DFT methods, where at least the innermost full electron

shell (referring to $1s \uparrow\downarrow$ electrons, equivalent to the K shell in spectroscopic characterization) is modeled by a modification of the potential describing the atomic nucleus, we include all core electrons into the calculations. We describe the various atomic environments of B in real space to prevent a disturbing overlap of dopant (i.e., B) wavefunctions, which is naturally missing in solids below the alloy threshold as would be presented here by Si borides SiB_n .^[15,24] Such overlaps can be prevented in reciprocal-space DFT methods only by adding a big vacuum gap around the supercell at great computational cost and thus at the expense of the size of the supercell. In real space, such overlaps do not exist. We invest the associated drop in computational cost into approximants of increased size, going literally to great lengths in terms of next-neighbor (nn) atoms around the B atom, thus describing the B environment to a realistic degree while keeping DFT calculations tractable.

There are several circumstances which render the assignment of B configurations in Si, SiO, and SiO₂ to K-shell signals in XANES spectroscopy significantly more complex as compared to phosphorus (P) in these materials.^[23]

We begin by looking at B on a Si site in bulk Si as the conventional acceptor state. Figure 3 shows us that there might be a minor peak at ≈ 192.35 eV that does not qualify for a reliable assignment to B acceptors in bulk Si, although the bulk-Si sample has a high density of such acceptors. To the best of our knowledge, the reason for the evasiveness of experimental data on the K-shell energy of B in a conventional acceptor configuration in Si has not been discussed yet in the literature. As a general hypothesis, we propose that the dipole transition moment as a key parameter for the oscillator strength of the core level transition in Fermi's golden rule for a Fano resonance (discrete K-shell transition to the conduction band continuum) is too small to allow for a signal to be detected for B concentrations below

the alloy limit mentioned later. This hypothesis is corroborated by the nearly covalent bond of B to Si (ionic bond character is $\approx 2\%$, using Allred–Rochow electronegativities).^[24] Another reason for the low transition moment of the K-shell transition of B may be the rather wide spread of K-shell core levels as compared to the same type of core levels with higher binding energy, e.g., 2143.7 eV for the K-shell signal of P as a donor in bulk Si.^[23] Such a wide spread of a core level over energy naturally depletes its resonant response when compared to a discrete final energy state of high density, where all levels of one chemical species in a certain configuration superimpose at exactly one transition energy. Partial fluorescence yield (PFY)-XANES characterization of B is further complicated by the close proximity of the K-shell signal of the B acceptor configuration to the signal of B dimers with partial or full H passivation (see Table 2 and Figure 3b). A clear separation cannot be achieved, simply due to the finite spread of B K-shell levels mentioned previously. As a result, the sensitivity of PFY-XANES to B as a very light element with a low K-shell energy of ≈ 192.3 eV as per calibration of DFT data is rather limited.

Another reason for the complexity of XANES spectra on B configurations in Si and related oxides is given by the more diverse locations of B in SiO₂. The ionic radius of B on an O site is close to the associated radius of O itself, viz., $r_B^{-0.04} = 0.85$ Å versus $r_O^{-1.08} = 0.92$ Å.^[25] In contrast, the atomic radius of Si in SiO₂ is $r_{\text{Si}}^{+2.16} = 0.75$ Å, whereas B on a Si site has merely 2/3 of the atomic radius with $r_B^{+1.66} = 0.45$ Å. These ratios of atomic radii combined with the higher Allred–Rochow electronegativity (EN) of B versus Si (2.01 vs 1.74)^[26] enables B to occupy Si as well as O sites in SiO and SiO₂, which has been demonstrated by B-doped SiO₂ characterized by capacitance–voltage (CV) and deep level transient spectroscopy (DLTS) scans in compound with DFT calculations.^[25] As for P, its atomic radius as donor on a Si site in SiO₂ differs from the

Table 2. Overview of all DFT-derived $1s \uparrow\downarrow$ electron binding energies and their experimental match. Also shown are the calculated net charge, q , at the B site, and the reference to the figure and graph showing the corresponding atomic configuration of B in the lattice.

E_{bind} [eV]	Q (B) [e]	Approximant (host lattice, site)/sample, specific configurations of 1nn atoms	Figure	Corresponding peak position observed in XANES [eV]
191.07	−0.15	B (SiO ₂ , O site)	4b	191.5 ^{a)}
191.86	−0.12	B (SiO, O site)	4d	191.7
191.99	−0.09	>B–B< (Si), 2× DB–Si	5a	192.0
192.04	+0.36	>B–OH (Si), substituting Si–Si	7b	192.0
192.34	−0.19	≡B (Si), 1× DB–Si; conventional acceptor	5d	192.35
192.35	−0.04	>B–B< (Si), 1× DB–Si, 1× H–Si	5b	192.35
192.37	−0.04	>B–B< (Si), 2× H–Si	5c	192.35
193.15	+0.56	B (Si), 2× –O–Si, 1× –Si, 1× DB–Si	7a	193.4
193.16	+0.35	B (SiO, Si site), 2× –O–Si, 1× –Si, 1× DB–Si	4c	193.4
193.48	+0.36	interstitial O=B–OH (SiO _x shell around NCs)	7c	193.4; 193.65
194.25	+0.78	B (SiO ₂ , Si site); confirmed in experiment ^[21,22] borosilicate glasses, ≡Si–O…B(–O–Si≡) ₃ ; sp^3 hybridization (tetrahedral B coordination) ^[21,22,51] borosilicate glasses, ≡Si–O…B(–O–Si≡) ₃ ; sp^3 hybridization (tetrahedral B coordination), and to ≡Si–O…B(–O–Si≡) ₃ ; sp^2 hybridization (trigonal B coordination) ^[21,22,51]	4a	194.25 ≈200 ≈204

^{a)}No articulate peak; minor possible peak signal at sample 6 nm-H only.

value of neutral Si by a considerable 44%, viz., $r_{\text{P}}^{+0.15} = 1.08 \text{ \AA} = 1.44 r_{\text{Si}}^{+2.16} = 0.75 \text{ \AA}$.^[26] Although an occupation of an O lattice site by P in SiO or SiO₂ is already unlikely due to its pentavalent bond configuration, its substantial oxidation enthalpy of $2\text{P} + 2\frac{1}{2}\text{O}_2 \rightarrow \text{P}_2\text{O}_5$ of 1493 kJ mol^{-1} (7.737 eV per P atom)^[26] and its high diffusion coefficient in Si^[9] allow P to form its own native oxide, reducing SiO₂ or SiO in the process. As for XANES, such findings are corroborated by the massive signal of the native P oxide P₂O₅ dwarfing the signal for P on Si sites in SiO₂, which strongly suggests the oxide phase separation of P mentioned earlier.^[23] The straightforward integration of B into SiO₂—and into other O-related B configurations discussed later—is corroborated by depth profiles of Si NC/SiO₂ superlattices (SLs) obtained from atom probe tomography (APT), where the majority of B atoms were located within SiO₂ and at the NC interface.^[3,9,11] As we shall see later, the phase separation of B in SiO₂ versus the formation of its native oxide B₂O₃ behaves the opposite way, with an oxide phase separation occurring only to a minor degree. Out of the 20 approximants calculated by DFT, we present the 11 relevant ones subsequently. Where instructive, we refer to the remaining 9 approximants in the context of the 11 approximants presented here. We have to conduct a calibration of $1s\uparrow\downarrow$ binding energies of B— $E_{1s\uparrow\downarrow}(\text{B})$ —to the peaks of XANES spectra presenting the binding energy of the K shell of B ($E_{\text{K}}(\text{B})$) in various electronic environments. We use the most prominent XANES peak of B on a Si site in SiO₂ at $E_{\text{K}}(\text{B}, \text{SiO}_2)$ to align $E_{1s\uparrow\downarrow}(\text{B})$ in the respective approximant (see, e.g., **Figure 4a**), arriving at a calibration factor of 1.042 for all $E_{1s\uparrow\downarrow}(\text{B})$ from DFT to match $E_{\text{K}}(\text{B})$ obtained by XANES. Such a calibration is also known from the alignment of Raman- and infrared (IR) frequencies obtained by DFT to respective experimental spectra,^[27,28] accounting for the approximate solution delivered inherently by DFT.^[29] All values of $E_{1s\uparrow\downarrow}(\text{B})$, the respective atomic environment and bond geometry, and the associated $E_{\text{K}}(\text{B})$ are shown in Table 2. From **Figure 3** it emerges that the assignment of $E_{1s\uparrow\downarrow}(\text{B})$ values obtained by DFT to $E_{\text{K}}(\text{B})$ in the XANES spectra is further complicated by several $E_{1s\uparrow\downarrow}(\text{B})$ values being very close to each other. Hence, we conducted a careful discrimination of such $E_{1s\uparrow\downarrow}(\text{B})$ values against their likely or experimentally documented occurrence in specific atomic environments (samples). However, a full deconvolution of DFT-backed XANES data as successfully conducted for P in the Si/SiO/SiO₂ system^[23] does not appear to be feasible for B.

We first evaluate our DFT results of B in SiO and SiO₂. As mentioned earlier, B can occupy Si as well as O lattice sites in both oxides, providing four atomic configurations (see **Figure 4**).

As discussed before, a phase separation of B₂O₃ versus SiO₂:B should hardly occur. This statement is corroborated by the low intensity of XANES peaks of B in borosilicate glasses and B₂O₃, occurring at $E_{\text{K}}(\text{B}) = 200$ and 204 eV, respectively (see **Figure 3a**). The formation of BO as an intermediate oxidation product^[30] is promoted by an O deficiency due to B being added to SiO (NC samples) or SiO₂ (sample SiO₂:B) *without* additional O to form a commensurate oxide, viz., B₂O₃. In terms of oxidation enthalpy, the value of B₂O₃ ($4\text{B} + 3\text{O}_2 \rightarrow 2\text{B}_2\text{O}_3 + 2547.2 \text{ kJ mol}^{-1}$, equivalent to 6.600 eV per B atom) does not suffice to induce a redox reaction along $2\text{B} + 6\text{SiO}_2 \rightarrow \text{B}_2\text{O}_3 + 6\text{SiO}$ in analogy to P,^[23] preventing B₂O₃ formation on a major scale altogether. In addition, the low diffusion constant of B in SiO₂ even at high temperature^[9] hampers the formation of B₂O₃ on a major scale as the nominal B concentration is too low for a true alloy phase to form those oxides.

From the magnified XANES spectra in **Figure 3b**, we see that B on an O site in SiO₂ (structure 4b) virtually does not occur, and is vastly outrun by the signal of B on a Si site in SiO₂ (structure 4a) for all samples containing SiO₂ in any form. We can therefore state that B on a lattice site in SiO₂ nearly always substitutes Si. A rather balanced ratio of B on O versus Si sites in SiO₂ as found by CV, DLTS, and DFT is based on an the *electrically active* B concentration in SiO₂ which is severely limited by a Coulomb blockade.^[25] The true physical B concentration on such sites in SiO₂ could thus not be characterized in the mentioned work. In contrast, DLTS is extremely sensitive (detecting sheet charge densities of $\approx 10^7 \text{ cm}^{-2}$), exceeding the detection limit of XANES (sheet densities of $\approx 10^{11} \text{ cm}^{-2}$ when taking $\approx 1\%$ of the integral of the B density over depth in **Figure 2**, corresponding to $\approx 0.01 \text{ at\%}$) by a factor of $\approx 10^4$, enabling DLTS to characterize such B configurations that cannot be detected by XANES. The B configurations in SiO will be discussed subsequently along with other O-related B configurations occurring in the suboxide shell around the pure Si NC.

We now look at B in Si, addressing both Si NCs and bulk Si. Due to the strong localization of the B $1s\uparrow\downarrow$ electrons, their binding energy $E_{1s\uparrow\downarrow}(\text{B})$ depends mainly on the 1nn atoms of B, with more distant host atoms only having a minor influence on

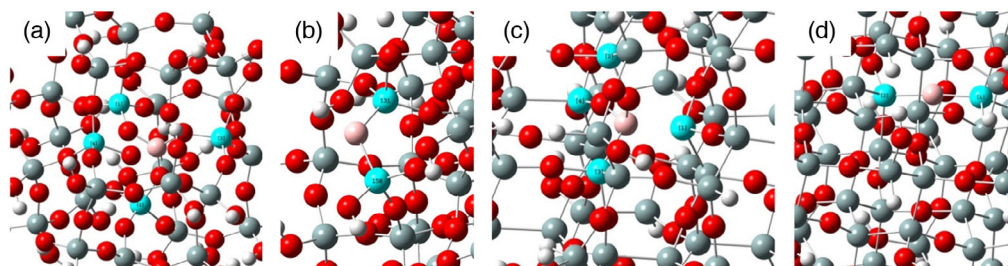


Figure 4. Relevant regions of DFT approximants showing B in SiO₂ and SiO. Atom colors are red for O, gray for Si, white for H, and pink for B. 1nn Si atoms of B are highlighted in cyan as a guide for atomic structure. a) B on Si site in SiO₂, featured by a Si₄₄BO₁₁₅H₅₆ approximant. b) B on O site in SiO₂, featured by a Si₄₅BO₁₁₆H₅₆ approximant. c) B on Si site in SiO, featured by a Si₇₃BO₉₀H₆₄ approximant. d) B on O site in SiO, featured by a Si₇₄BO₈₉H₆₄ approximant.

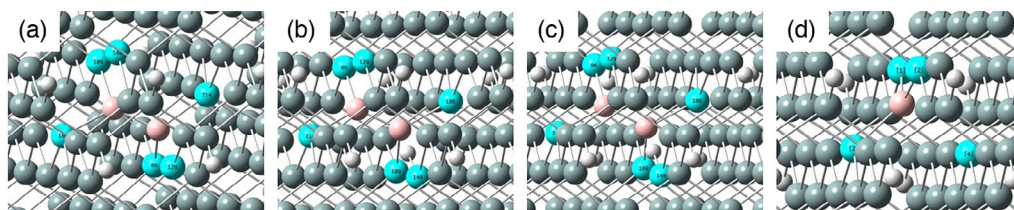


Figure 5. Relevant regions of DFT approximants showing B in H-terminated 2.2 nm Si NCs (nominal Si_{286} core) without involving O atoms. Such approximants have Si around B up to $7 \pm 2\text{nn}$ positions, emulating a bulk Si environment for strongly localized electronic states with high binding energy, such as $1s$ core levels of B. a) $\text{Si}_{284}\text{H}_{144}$ NC with two central adjacent Si atoms replaced by a B dimer, resulting in two 1nn Si atoms with one DB each— $\text{Si}_{284}(>\text{B}-\text{B}<)\text{H}_{144}$, $2 \times$ 1nn-Si-DB. b) Same $\text{Si}_{284}\text{H}_{144}$ NC as in (a), whereby one of the DBs is passivated with $\text{H}-\text{Si}_{284}(>\text{B}-\text{B}<)\text{H}_{144}$, 1nn Si DB, 1nn Si H. c) The same NC approximant as in (a), with both 1nn Si atoms to B being passivated with $\text{H}-\text{Si}_{284}(>\text{B}-\text{B}<)\text{H}_{144}$, $2 \times$ 1nn Si H. d) Nominal-doping case where B is on an Si site and one 1nn Si has a DB toward B, which forms the acceptor state in bulk $\text{Si}-\text{Si}_{285}\text{BH}_{144}$, 1nn Si DB. As for atom colors, we refer the reader to Figure 4.

$E_{1s\uparrow\downarrow}(\text{B})$. Dimers of the form $>\text{B}-\text{B}<$ ($>$ and $<$ stand for bridge bonds between Si atoms) are readily formed within Si at high B concentrations.^[18–20] We consider three $>\text{B}-\text{B}<$ configurations in Si, differing in the passivation of the two dangling bonds (DBs) of the two 1nn Si atoms not bonded to B: fully defective ($2 \times$ 1nn Si-DB, structure 5a), partially passivated (1nn Si-DB and 1nn Si-H, structure 5b), and fully passivated ($2 \times$ 1nn Si-H, structure 5c) (see Figure 5a–c, respectively). From Figure 3b, we see that the fully defective $>\text{B}-\text{B}<$ configuration has a value of $E_{1s\uparrow\downarrow}(\text{B})$ that is ≈ 0.37 eV lower when compared to the partially and fully passivated $>\text{B}-\text{B}<$ configuration. Hydrogen (H) has an EN of 2.2 and is thus only marginally more anionic to Si (EN = 1.74) than B (EN = 2.01).^[26] However, the crucial factor is the electron affinity X , with $X(\text{B}) = -0.277$ eV versus $X(\text{H}) = -0.756$ eV.^[26] Therefore, H delivers a slightly higher electron relaxation when compared to B, resulting in an electron flow away from the B dimer toward the H atom(s) passivating the Si DB(s). Consequently, the partially and fully passivated $>\text{B}-\text{B}<$ configurations (structures 5b and 5c) ionize B atoms slightly less negatively when compared to the unpassivated $>\text{B}-\text{B}<$ configuration (structure 5a); see atomic charges of B in Table 2. This change in ionization of the B atoms affects the $E_{1s\uparrow\downarrow}(\text{B})$ level via a diminished Coulomb repulsion term within the nominal cumulative electron shell ($1s\uparrow\downarrow$, $2s\uparrow\downarrow 2p\uparrow$), corresponding to a shift of $E_{1s\uparrow\downarrow}(\text{B})$ by ≈ 0.37 eV. Unfortunately, the $E_{1s\uparrow\downarrow}(\text{B})$ of this B dimer configuration nearly coincides with the $E_{1s\uparrow\downarrow}(\text{B})$ of a $>\text{B}-\text{OH}$ bridge substituting a bond Si–Si; see structure 7b in Table 2. Therefore, it is impossible to discriminate between both B configurations when using merely respective $E_{1s\uparrow\downarrow}(\text{B})$ values.

However, the $>\text{B}-\text{OH}$ configuration arguably fits to the evolution of the XANES peaks with NC diameter while not occurring in bulk Si at all as discussed subsequently for B–O-related species in or near pure Si. We therefore conclude here that all three $>\text{B}-\text{B}<$ configurations appear to occur with comparable probabilities (XANES peak areas). The higher $E_{1s\uparrow\downarrow}(\text{B})$ levels of partially/fully passivated $>\text{B}-\text{B}<$ configurations suggest their increased occurrence on thermodynamic grounds. In contrast, the additional energy required for saturating DBs at 1nn Si atoms with H due to the proximity of H atoms to $>\text{B}-\text{B}<$ appears to cancel the energy gain by H passivation. The aforementioned situation is well met by the 1nn Si DB of a conventional B acceptor configuration in Si ($\text{Si}_3\equiv\text{B}\cdots\text{DB}-\text{Si}\equiv\text{Si}_3$)—see Figure 5d—which is not passivated to a notable degree by H, resulting in an inactivated acceptor state. Such a situation clearly does not occur in bulk Si: Any H anneal for passivating Si solar cells would result in the inactivation of B-based background doping, jeopardizing the working principle of the solar cell by increasing its series resistance to prohibitive values. This statement is supported by the distance between the B atom and its 1nn Si with an active versus a H-passivated DB, yielding 2.68 and 2.94 Å, respectively. This increase in the distance between the B atom and its 1nn Si by $\approx 10\%$ yields an energy penalty which exceeds the energy gain by passivating the Si DB with H, again confirming the aforementioned considerations from a theoretical viewpoint. Figure 6 gives an impression of the associated lattice distortion.

The conventional B acceptor configuration in Si (structure 5d) has an $E_{1s\uparrow\downarrow}(\text{B})$ that coincides with the values of partially and fully

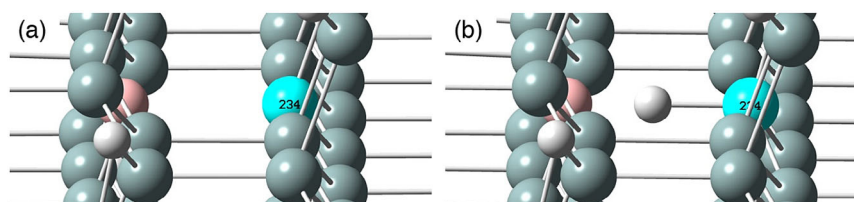


Figure 6. a) Conventional B acceptor configuration in Si using the same approximant as in Figure 5d ($\text{Si}-\text{Si}_{285}\text{BH}_{144}$, 1nn Si DB), shown along the $[11\bar{1}]$ vector. b) The same approximant with the 1nn Si DB passivated with H shown along the same lattice vector shows a significant displacement of the highlighted 1nn Si atom. This shows the local lattice distortion occurring by H passivation of the acceptor state, the former requiring more energy than is gained by the latter as empirically proven, e.g., for H-passivated Si solar cells based on B-doped wafers. The relevant Si atom is highlighted in cyan; for other atom colors we refer the reader to Figure 4.

passivated $>B-B<$ configurations, therefore not allowing an assignment to either B configuration from a theoretical viewpoint. However, because the experimental verification of the conventional B acceptor configuration in bulk Si (sample Si:B) by XANES led to only a minute bump signal as mentioned in the Results section, we assume that the XANES peak we obtained is overwhelmingly due to partially/fully H-passivated B dimers. In that context, we would like to point out that B densities of ≥ 0.3 at% or $1.5 \times 10^{20} \text{ cm}^{-3}$ in bulk Si convert the electronic structure of the latter into a semimetal.^[31]

The $>B-B<$ configurations shown in Figure 5 introduce a considerable amount of local lattice distortion, mainly by the bonds B–B ($\approx 1.75 \text{ \AA}$) and B–Si bonds ($\approx 2.13 \text{ \AA}$) being notably smaller to the nominal Si–Si bonds ($\approx 2.38 \text{ \AA}$). It is therefore conceivable that a reactive species such as O can participate in alternative B configurations by breaking the bond B–Si or Si–Si at high temperature as brought about by a dopant activation or Si segregation anneal of SiO to form Si NCs in SiO₂. A single B configuration in analogy to the conventional B acceptor—cf., Figure 5d—can be established with less lattice strain and considerable energy gain by the oxidation enthalpy brought about by two bonds Si–B substituted by O bridge bonds ($>O$), yielding $\equiv\text{Si}-\text{B}(-\text{O}-\text{Si}\equiv)_2\cdots\text{DB}-\text{Si}\equiv$ as shown in Figure 7a. At $E_{1s\uparrow\downarrow}(\text{B}) = 193.15 \text{ eV}$, there is a shoulder in the XANES spectrum of sample 6 nm-H, which is $\approx 0.25 \text{ eV}$ shifted to higher $E_K(\text{B})$, whereas only one broad small peak is visible for sample 3 nm-H. The XANES signal of sample 3 nm-H also appears to contain the other two B configurations discussed later. From Figure 3b, we can derive that B configurations of the type shown in Figure 7a occur only in highly B-doped NC samples, whereby the associated XANES peak gets more articulate with increasing NC diameter. This relation clearly corresponds with the thickness of the suboxide (SiO_x) shell around the NC, which is at least 6 Å thick^[32] and increases with NC diameter.^[33,34] We can thus locate the $\equiv\text{Si}-\text{B}(-\text{O}-\text{Si}\equiv)_2\cdots\text{DB}-\text{Si}\equiv$ configuration to the SiO_x shell with small x values where a sizeable amount of Si–Si bonds is still present, thus at the transition to the pure Si NC lattice. The associated XANES peak grows with NC diameter simply by the corresponding increase in NC surface. Another configuration that bridges Si–Si bonds is given by $>B-OH$ at binding energy $E_{1s\uparrow\downarrow}(\text{B}) = 192.04 \text{ eV}$; see Figure 7b for an illustration and Figure 3b for the XANES peak at $E_K(\text{B}) = 192.0 \text{ eV}$. Such a configuration essentially requires a SiO_x shell with small x values as an environment to exist because the B bridge separates the two

1nn Si atoms by $\approx 3.66 \text{ \AA}$. This environment exists not quite as near to the pure Si NC surface as found for the $\equiv\text{Si}-\text{B}(-\text{O}-\text{Si}\equiv)_2\cdots\text{DB}-\text{Si}\equiv$ configuration, therefore near the surface of the pure Si NC within the SiO_x shell. Another indicator for this location is given by the immense growth of the associated XANES peak with NC diameter, viz., going from hardly noticeable for sample 3 nm-H to considerable intensity for sample 6 nm-H, where the SiO_x shell is significantly thicker.^[33,34] Another XANES peak related to B in a SiO_x environment is given by B on a Si site in SiO, a configuration which is shown in Figure 4c. Its $E_{1s\uparrow\downarrow}(\text{B})$ value of 193.16 eV is indistinguishable in experiment from the $\equiv\text{Si}-\text{B}(-\text{O}-\text{Si}\equiv)_2\cdots\text{DB}-\text{Si}\equiv$ configuration discussed earlier. To add, both configurations share the SiO_x phase as their optimum environment.

The last configuration of B involving O only in its proximity is shown in Figure 7c, displaying the only case where B does not bond to the local lattice. Appearing strange at first glance, the interstitial $\text{O}=\text{B}-\text{OH}$ molecule has its origin in the presence of residual O in the proximity of B at high temperatures, where B acts as a strong reduction agent. For comparison, forming of boron nitride (BN) along $2\text{B} + \text{N}_2 \rightarrow 2\text{BN} + 510 \text{ kJ mol}^{-1}$ (4.14 eV/B atom) takes place at 900°C , whereas the equivalent reaction of Si with N₂ does not occur below $\approx 1200^\circ\text{C}$.^[26] During the anneal at 1100°C , BOOH can form if reactive/residual O is present in the sample, which is likely the case for SiO_x precursor layers where Si NCs are formed. A corresponding XANES peak to $E_{1s\uparrow\downarrow}(\text{B}) = 193.48 \text{ eV}$ appears to be situated at $E_K(\text{B}) = 193.65 \text{ eV}$, whereby its dependence on NC size plainly shows that the location of BOOH is within the SiO_x shell surrounding the Si NCs as is the case in previous O-related B configurations. Once again, the broad peak of sample 3 nm-H does not allow us to discriminate between signals originating from BOOH versus B on an Si site in SiO versus the $\equiv\text{Si}-\text{B}(-\text{O}-\text{Si}\equiv)_2\cdots\text{DB}-\text{Si}\equiv$ configuration. The presence of N₂ during annealing along with reactive/residual O might also lead to a formation of BN, although the formation of O-related B configurations outruns BN formation in terms of reactivity and reaction enthalpy by far.^[26]

4. Conclusion

B-doped, SiO₂-embedded Si nanocrystal samples and respective SiO₂:B and bulk-Si:B reference samples were studied by XANES at the B K-edge and by real-space DFT. The XANES spectra of the

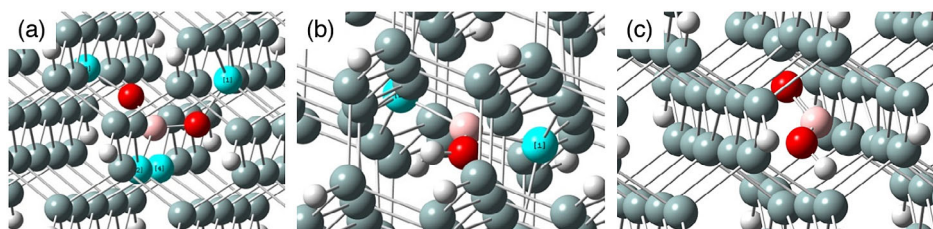


Figure 7. Relevant regions of DFT approximants showing B in H-terminated 2.2 nm Si NC (nominal Si₂₈₆ core) with participation of O atoms. a) We start with the same NC approximant as in Figure 5c, whereby two of the three direct bonds of B to its 1nn Si are bridged by $\text{O}-\text{Si}_{285}(-\text{B}(-\text{O}-)_2)\text{H}_{144}$, 1nn Si DB. b) The nominal Si₂₈₆H₁₄₄ approximant with one Si–Si bond broken up and bridged by $>B-OH-\text{Si}_{286}\text{H}_{144}$ with Si–B(OH)–Si substituted for Si–Si. c) At high temperatures, B can form BOOH ($\text{O}=\text{B}-\text{OH}$) as a precursor to boric acid ($\text{B}(\text{OH})_3$, sum formula H_3BO_3) being created under O deficiency in Si, as shown here in the nominal Si₂₈₆H₁₄₄ NC. As for atom colors, we refer the reader to Figure 4.

Si NC samples with low average B concentration (0.24–0.31 at%) feature mainly one peak at 194.25 eV, which is attributed to B on a Si site in SiO₂ (structure 4a). Increasing the average B concentration to 0.66–0.88 at% leads to the occurrence of B dimers with Si bridge bonds and (un)passivated Si dangling bonds with XANES peaks at 192.00–192.35 eV (structures 5a–c). Also, broad peaks at 200 and 204 eV occur, which are typical features of borosilicate glasses and B zeolites. Finally, two features on the shoulder of the 194.25 eV peak occur at 193.65 and 193.4 eV, which can be attributed to either BOOH (structure 7c) or a B atom where two of the three Si–B bonds to the 1nn Si are bridged by O (structure 7a). All of these high-[B] features demonstrate that an excessive amount of B does not enrich the B concentration in the Si NCs but forms new configurations that are inherently incompatible with electronic doping. Therefore, it is concluded that B in the Si NC/SiO₂ system is predominantly incorporated in the SiO_x transition shell at the Si/SiO₂ interface with a partial O coordination as well as in the SiO₂ matrix surrounding the NCs, provided the B concentration remains below the threshold to hyperdoping and the formation of Si borides. The findings of our combined XANES-DFT study are well in accordance with recent results about the location of B in Si NCs obtained from APT,^[3,9,11] current–voltage measurements,^[3] and high-energy X-ray diffraction.^[10]

The mounting evidence that electronic B doping of low nanoscale Si nanostructures fails for a multitude of fundamental physical reasons requires the investigation of alternative strategies that do not rely on classical impurity doping. Acceptor modulation doping of SiO₂^[25,35] and the electronic structure shift in low nanoscale intrinsic Si by ultrathin coating with SiO₂ versus Si₃N₄^[36,37] are two such strategies which allow us to induce a strong electron or hole dominance in analogy to conventional doping without its detrimental side effects and associated size limits.

5. Experimental Section

Sample Fabrication: Multiple bilayer stacks of B-doped Si-rich oxide (SRO:B, with stoichiometry parameter SiO_{x≈1.0}) and SiO₂ were deposited on wet-chemically cleaned Si substrates (n-type, 5–25 Ω cm) by plasma-enhanced chemical vapor deposition (PECVD) using SiH₄, 10% B₂H₆/SiH₄, O₂, and Ar.^[3,38] At first, a 30 nm thick SiO₂ buffer layer was deposited on the wafers to prevent diffusion of B dopants into the lowly phosphorus-doped substrates. Note that a diffusion length of only ≈7 nm for B in SiO₂ was reported before for a comparable sample system and process conditions.^[9] A total of 50 bilayers of either 3 nm or 6 nm SRO:B and 3 nm SiO₂ were deposited and capped with a 10 nm thick SiO₂ layer. Two different nominal B concentrations in the SRO:B layer were used, 1.32 and 0.47 at%.^[3] SiO₂:B reference samples were fabricated with 225 nm thickness, 0.8 and 0.25 at% B concentration, and the same buffer/capping layers. All B concentrations were determined by molecular Cs⁺ SIMS (MCs⁺-SIMS).^[3] After deposition, the samples were annealed in a quartz glass tube furnace at 1100 °C for 1 h in a high-purity N₂ atmosphere and subsequently at 450 °C for 1 h in pure H₂ to grow and crystallize the Si NCs and to passivate Si NC/SiO₂ interface defects, respectively.^[39]

For comparison to ionized B dopants in bulk Si, a reference sample was prepared by ion implantation. A boron dose of $1 \times 10^{16} \text{ cm}^{-2}$ was implanted at 20 keV (resulting in a projected range of ≈80 nm where the initial B concentration reached ≈ 10^{21} cm^{-3}) and subsequently annealed at 1000 °C for 45 min. After annealing the sample was etched in a hydrofluoric acid (HF) solution to remove any silicon oxide grown

in the furnace. According to four-point-probe measurements, a sheet resistance of $19 \Omega \square^{-1}$ was obtained. No additional HF dip was performed directly before XANES measurements so that the sample was passivated with a native oxide.

Measurements: PL was measured using a LN₂-cooled CCD camera attached to a single grating monochromator with excitation by a HeCd laser (325 nm, ≈3 mW cm⁻²). Electrochemical capacitance–voltage (ECV) profiling was conducted using a CVP21 system from WEP. XANES at the B K-edge was measured at IQMT's soft X-ray analytics facility WERA at the KIT synchrotron light source KARA, Karlsruhe, Germany. The photon-energy resolution was set to 100 meV, and a windowless four-element silicon drift detector was used to record XANES spectra in PFY detection mode, with the detection window set around the B 1s fluorescence. A NiO reference sample measured in parallel to all B K spectra provided an energy reference signal (Ni L₃ edge in fourth order). It enables correction of a “global shift,” which amounted to ≈120 meV. A number of individual spectra showed a maximum shift of (+40, –80) meV relative to this “global shift.” These relative shifts for individual spectra were too small to influence the results, where energy distances of 300 meV appear important, and thus were not corrected for here. The B 1s PFY-XANES sampling depth in Si and SiO₂ was ≈30 and 50 nm, respectively. A strong spectral background (that may include scattering effects) was removed in the energy windows shown, and the spectra were corrected for variations in the incoming intensity, I_0 . The fluorescence efficiency is low at B 1s, so for some samples, many individual spectra were averaged to increase the signal-to-noise (S/N) ratio.

DFT Calculations: Real-space calculations were conducted with a molecular orbital basis set (MO-BS) and Hartree-Fock (HF)/DFT methods, using the Gaussian09 program package^[40] with the GaussView program^[41] for visualization. Initially, the MO-BS wavefunction ensemble was tested and optimized for describing the energy minimum of the system (variational principle; stable = opt) with the HF method.^[42–44] Exact exchange interaction inherent to HF is crucial in obtaining accurate bond geometries.^[36] As MO-BS, the Gaussian type 3-21G MO-BS (HF/3-21G) was used.^[45] The HF/3-21G route was used for the structural optimization of the approximants to arrive at their most stable configuration (maximum integral over all bond energies); root mean square (RMS) and peak force convergence limits were 8 and 12 meV Å⁻¹, (300 and 450 μHa Å⁻¹), respectively. Optimized geometries were used to calculate their electronic structure by testing and optimizing the MO-BS wavefunction ensemble with the nonlocal B3LYP hybrid DF method^[46–48] and the Gaussian type 6-31G(d) MO-BS, which contains *d*-polarization functions (B3LYP/6-31G(d))^[49] for all chemical elements. For all calculations, tight convergence criteria were set to the self-consistent field routine and no symmetry constraints to MOs were applied. Ultrafine integration grids were used throughout. The supporting information to König et al.^[36,50] contains accuracy assessments.

Acknowledgements

D.H. thanks the Alexander von Humboldt Foundation for a Feodor Lynen Fellowship and Return Fellowship and acknowledges funding by the German Research Foundation DFG (project HI 1779/3-1). Furthermore, D.H. acknowledges the Laboratory for Nanotechnology at IMTEK (University of Freiburg, Germany) for providing access to processing and analysis equipment for Si nanocrystal samples. The authors thank Dr. Tom Ratcliff and Prof. Robert Elliman (ANU, Canberra) for providing the B-implanted Si reference sample and Dr. Josua Stuckelberger (ANU, Canberra) for support with the ECV measurements. D.K. acknowledges the 2018 Theodore-von-Kärman Fellowship of RWTH Aachen University, Germany, and wishes to thank J. Rudd for administrating the compute clusters of the IMDC at UNSW, and for compute time provided by the IMDL at the Raijin mainframe, NCI, ANU, Canberra, Australia. The Karlsruhe synchrotron light source KARA and the Karlsruhe Nano Micro Facility (KNMF) are gratefully acknowledged for the provision of beamtime.

Open access funding enabled and organized by Projekt DEAL.

Conflict of Interest

The authors declare no conflict of interest.

Data Availability Statement

The data that support the findings of this study are available from the corresponding author upon reasonable request.

Keywords

boron doping, nanocrystals, quantum dots, silicon

Received: December 23, 2020

Revised: March 1, 2021

Published online:

-
- [1] M. Fujii, S. Hayashi, K. Yamamoto, *J. Appl. Phys.* **1998**, *83*, 7953.
 [2] G. Zatyb, A. Podhorodecki, X. J. Hao, J. Misiewicz, Y. S. Shen, M. A. Green, *Opt. Express* **2010**, *18*, 22004.
 [3] D. Hiller, J. López-Vidrier, S. Gutsch, M. Zacharias, M. Wahl, W. Bock, A. Brodyanski, M. Kopnarski, K. Nomoto, J. Valenta, D. König, *Sci. Rep.* **2017**, *7*, 8337.
 [4] D. Hiller, J. López-Vidrier, K. Nomoto, M. Wahl, W. Bock, T. Chlouba, F. Trojánek, S. Gutsch, M. Zacharias, D. König, P. Malý, M. Kopnarski, *Beilstein J. Nanotechnol.* **2018**, *9*, 1501.
 [5] R. Limpens, H. Sugimoto, N. R. Neale, M. Fujii, *ACS Photonics* **2018**, *5*, 4037.
 [6] X. Pi, X. Chen, D. Yang, *J. Phys. Chem. C* **2011**, *115*, 9838.
 [7] B. Puthen-Veettil, L. Wu, X. Jia, Z. Lin, T. Zhang, T. Yang, C. Johnson, D. McCamey, G. Conibeer, I. Perez-Würfl, *Appl. Phys. Lett.* **2014**, *105*, 222108.
 [8] R. Guerra, S. Ossicini, *J. Am. Chem. Soc.* **2014**, *136*, 4404.
 [9] K. Nomoto, S. Gutsch, A. V. Ceguerra, A. Breen, H. Sugimoto, M. Fujii, I. Perez-Wurfl, S. P. Ringer, G. Conibeer, *MRS Commun.* **2016**, *6*, 283.
 [10] K. I. Hunter, N. Bedford, K. Schramke, U. R. Kortshagen, *Nano Lett.* **2020**, *20*, 852.
 [11] R. Demoulin, D. Muller, D. Mathiot, P. Pareige, E. Talbot, *Phys. Status Solidi RRL* **2020**, *14*, 2000107.
 [12] N. J. Kramer, K. S. Schramke, U. R. Kortshagen, *Nano Lett.* **2015**, *15*, 5597.
 [13] Z. Ni, X. Pi, S. Zhou, T. Nozaki, B. Grandidier, D. Yang, *Adv. Opt. Mater.* **2016**, *4*, 700.
 [14] S. Zhou, Z. Ni, Y. Ding, M. Sugaya, X. Pi, T. Nozaki, *ACS Photonics* **2016**, *3*, 415.
 [15] D. Narducci, B. Lorenzi, X. Zianni, N. Neophytou, S. Frabboni, G. C. Gazzadi, A. Roncaglia, F. Suriano, *Phys. Status Solidi A* **2014**, *211*, 1255.
 [16] X. J. Hao, E.-C. Cho, C. Flynn, Y. S. Shen, S. C. Park, G. Conibeer, M. A. Green, *Sol. Energy Mater. Sol. Cells* **2009**, *93*, 273.
 [17] S. Solmi, F. Baruffaldi, R. Canteri, *J. Appl. Phys.* **1991**, *69*, 2135.
 [18] A. Vailionis, G. Glass, P. Desjardins, D. G. Cahill, J. E. Greene, *Phys. Rev. Lett.* **1999**, *82*, 4464.
 [19] D. De Salvador, G. Bisognin, M. Di Marino, E. Napolitani, A. Carnera, H. Graoui, M. A. Foad, F. Boscherini, S. Mirabella, *Appl. Phys. Lett.* **2006**, *89*, 241901.
 [20] D. De Salvador, G. Bisognin, M. Di Marino, E. Napolitani, A. Carnera, S. Mirabella, E. Pecora, E. Bruno, F. Priolo, H. Graoui, M. A. Foad, F. Boscherini, *J. Vac. Sci. Technol. B* **2008**, *26*, 382.
 [21] M. E. Fleet, S. Muthupari, *J. Non-Cryst. Solids* **1999**, *255*, 233.
 [22] J. A. van Bokhoven, C. Lamberti, *Coord. Chem. Rev.* **2014**, *277*, 275.
 [23] D. König, S. Gutsch, H. Gnaser, M. Wahl, M. Kopnarski, J. Göttlicher, R. Steininger, M. Zacharias, D. Hiller, *Sci. Rep.* **2015**, *5*, 9702.
 [24] A. F. Holleman, N. Wiberg, *Inorganic Chemistry*, Wiley & Sons, New York **2001**, p. 93.
 [25] D. König, D. Hiller, S. Smith, *Phys. Rev. Appl.* **2018**, *10*, 054034.
 [26] A. F. Holleman, E. Wiberg, N. Wiberg, *Lehrbuch der Anorganischen Chemie*, 101 ed., Walter de Gruyter, Berlin **1995**.
 [27] W. Rudolph, *Z. Phys. Chem.* **1996**, *194*, 73.
 [28] C. C. Pye, W. W. Rudolph, *J. Phys. Chem. A* **1998**, *102*, 9933.
 [29] Richard M. Martin, *Electronic Structure Theory*, 1st ed., Cambridge University Press, Cambridge **2004**.
 [30] R. J. Mulliken, *Phys. Rev.* **1925**, *25*, 259.
 [31] G. L. Pearson, J. Bardeen, *Phys. Rev.* **1949**, *75*, 865.
 [32] K. T. Queeney, M. K. Weldon, J. P. Chang, Y. J. Chabal, A. B. Gurevich, J. Sapjeta, R. L. Opila, *J. Appl. Phys.* **2000**, *87*, 1322.
 [33] A. Zimina, S. Eisebitt, W. Eberhardt, J. Heitmann, M. Zacharias, *Appl. Phys. Lett.* **2006**, *88*, 163103.
 [34] D. Hiller, S. Goetze, F. Munnik, M. Jivanescu, J. W. Gerlach, J. Vogt, E. Pippel, N. Zakharov, A. Stesmans, M. Zacharias, *Phys. Rev. B* **2010**, *82*, 195401.
 [35] D. König, D. Hiller, S. Gutsch, M. Zacharias, S. Smith, *Sci. Rep.* **2017**, *7*, 46703.
 [36] D. König, D. Hiller, N. Wilck, B. Berghoff, M. Müller, S. Thakur, G. Di Santo, L. Petaccia, J. Mayer, S. Smith, J. Knoch, *Beilstein J. Nanotechnol.* **2018**, *9*, 2255.
 [37] D. König, N. Wilck, D. Hiller, B. Berghoff, A. Meledin, G. Di Santo, L. Petaccia, J. Mayer, S. Smith, J. Knoch, *Phys. Rev. Appl.* **2019**, *12*, 054050.
 [38] J. Laube, S. Gutsch, D. Hiller, M. Bruns, C. Kübel, C. Weiss, M. Zacharias, *J. Appl. Phys.* **2014**, *116*, 223501.
 [39] A. M. Hartel, D. Hiller, S. Gutsch, P. Löper, S. Estradé, F. Peiró, B. Garrido, M. Zacharias, *Thin Solid Films* **2011**, *520*, 121.
 [40] M. J. Frisch, G. W. Trucks, H. B. Schlegel, G. E. Scuseria, M. A. Robb, J. R. Cheeseman, G. Scalmani, V. Barone, G. A. Petersson, H. Nakatsuji, X. Li, M. Caricato, A. Marenich, J. Bloino, B. G. Janesko, R. Gomperts, B. Mennucci, H. P. Hratchian, J. V. Ortiz, A. F. Izmaylov, J. L. Sonnenberg, D. Williams-Young, F. Ding, F. Lipparini, F. Egidi, J. Goings, B. Peng, A. Petrone, T. Henderson, D. Ranasinghe, et al., *Gaussian09, Revision D.01*, Gaussian, Inc., Wallingford, CT **2010**.
 [41] R. Dennington, T. Keith, J. Millam, *GaussView 5.0.8*, Semichem Inc., Shawnee Mission, KS **2009**.
 [42] D. R. Hartree, *Proc. Camb. Philos. Soc.* **1928**, *24*, 89.
 [43] D. R. Hartree, *Proc. Camb. Philos. Soc.* **1928**, *24*, 111.
 [44] V. Fock, *Z. Phys.* **1930**, *61*, 126.
 [45] M. S. Gordon, J. S. Binkley, J. A. Pople, W. J. Pietro, W. J. Hehre, *J. Am. Chem. Soc.* **1982**, *104*, 2797.
 [46] A. D. Becke, *Phys. Rev. A* **1988**, *38*, 3098.
 [47] C. Lee, W. Yang, R. G. Parr, *Phys. Rev. B* **1988**, *37*, 785.
 [48] A. D. Becke, *J. Chem. Phys.* **1993**, *98*, 5648.
 [49] M. M. Francl, W. J. Pietro, W. J. Hehre, *J. Chem. Phys.* **1982**, *77*, 3654.
 [50] D. König, D. Hiller, S. Gutsch, M. Zacharias, *Adv. Mater. Interfaces* **2014**, *1*, 1400359.
 [51] M. E. Fleet, S. Muthupari, *Am. Mineral.* **2000**, *85*, 1009.